Ⓔ

Fault-Scaling Relationships Depend on the Average Fault-Slip Rate

by John G. Anderson, Glenn P. Biasi,[*] and Steven G. Wesnousky

Abstract   This study addresses whether knowing the slip rate on a fault improves estimates of magnitude (M_w) of shallow continental surface-rupturing earthquakes. Based on 43 earthquakes from the database of Wells and Coppersmith (1994), Anderson *et al.* (1996) suggested previously that the estimates of M_w from rupture length (L_E) are improved by incorporating the slip rate of the fault (S_F). We re-evaluate this relationship with an expanded database of 80 events, which includes 56 strike-slip, 13 reverse-, and 11 normal-faulting events. When the data are subdivided by fault mechanism, magnitude predictions from rupture length are improved for strike-slip faults when slip rate is included but not for reverse or normal faults. Whether or not the slip-rate term is present, a linear model with $M_w \sim \log L_E$ over all rupture lengths implies that the stress drop depends on rupture length—an observation that is not supported by teleseismic observations. We consider two other models, including one we prefer because it has constant stress drop over the entire range of L_E for any constant value of S_F and fits the data as well as the linear model. The dependence on slip rate for strike-slip faults is a persistent feature of all considered models. The observed dependence on S_F supports the conclusion that for strike-slip faults of a given length, the static stress drop, on average, tends to decrease as the fault-slip rate increases.

Electronic Supplement: Table of earthquakes and parameters.

Introduction

Models for estimating the possible magnitude of an earthquake from geological observations of the fault length are an essential component of any state-of-the-art seismic-hazard analysis. The input to either a probabilistic or deterministic seismic-hazard analysis requires geological constraints because the duration of instrumental observations of seismicity is too short to observe the size and to estimate the occurrence rates of the largest earthquakes (e.g., Allen, 1975; Wesnousky *et al.*, 1983). Thus, wherever evidence in the geological record suggests earthquake activity, it is essential for the seismic-hazard analysis to consider the hazard from that fault, and an estimate of the magnitude of the earthquake (M_w) that might occur on the fault is an essential part of the process. The primary goal of this study is to determine if magnitude estimates that are commonly estimated from fault length (L_E) can be improved by incorporating the slip rate (S_F) of the fault.

Numerous models for estimating magnitude from rupture length have been published. Early studies were by Tocher (1958) and Iida (1959). Wells and Coppersmith (1994) published an extensive scaling study based on 244 earthquakes.

Some of the more recent studies include Anderson *et al.* (1996), Hanks and Bakun (2002, 2008), Shaw and Wesnousky (2008), Blaser *et al.* (2010), Leonard (2010, 2012, 2014), and Strasser *et al.* (2010). For probabilistic studies and for earthquake source physics, it is valuable to try to reduce the uncertainty in these relations. Motivated by Kanamori and Allen (1986) and Scholz *et al.* (1986), Anderson *et al.* (1996; hereafter, AWS96) investigated whether including the fault-slip rate on a fault improves magnitude estimates given rupture length. They found that it does, and proposed the relationship $M_w = 5.12 + 1.16 \log L_E - 0.20 \log S_F$, thus indicating that slip rate is a factor. A physical interpretation of a significant dependence on slip rate is that, for a common rupture length, faults with higher slip rates tend to have smaller static stress drop. Since the publication of AWS96, the number of earthquakes with available magnitude, rupture length, and slip-rate estimates has approximately doubled. This article considers whether these new data improve or modify the conclusions from the earlier study.

One consideration in developing a scaling model is that seismological observations have found stress drop in earthquakes to be practically independent of magnitude. Kanamori and Anderson (1975) is one of the early papers to make this observation. Recent studies that have supported

*Now at U.S. Geological Survey, 525 S. Wilson Avenue, Pasadena, California 91106; gbiasi@usgs.gov.

Table 1
Earthquakes from 1968–2011 Used in This Study

Event Number	Event Name	Event Date (yyyy/mm/dd)	M_w	Rupture Length (km)	Slip Rate (mm/yr)	Mechanism*
2	Fukushima-Hamadori, Japan	2011/04/11	6.7	15	0.02	N
4	Yushu, China	2010/04/14	6.8	52	12	S
5	El Mayor–Cucapah	2010/04/04	7.3	117	2.5	S
6	Wenchuan, China	2008/05/12	7.9	240	1.3	R
7	Kashmir, Pakistan	2005/10/08	7.6	70	3.1	R
8	Chuya, Russia (Gorny Altai)	2003/09/27	7.2	70	0.5	S
9	Denali, Alaska	2002/11/03	7.8	340	12.4	S
10	Kunlun, China	2001/11/14	7.7	450	10	S
11	Düzce, Turkey	1999/11/12	7.1	40	15	S
12	Hector Mine, California	1999/10/16	7.1	48	0.6	S
13	Chi-Chi, Taiwan	1999/09/21	7.7	72	12.9	R
14	İzmit, Turkey	1999/08/17	7.5	145	12	S
15	Fandoqa, Iran	1998/03/14	6.6	22	2	S
16	Manyi, China	1997/11/08	7.4	170	3	S
17	Sakhalin Island (Neftegorsk), Russia	1995/05/27	7.0	40	4	S
18	Northridge, California	1994/01/17	6.7	21	0.4	R
19	Landers, California	1992/06/28	7.2	77	0.4	S
20	Luzon, Philippines	1990/07/16	7.7	112	15	S
21	Rudbar, Iran	1990/06/20	7.4	80	1	S
22	Loma Prieta, California	1989/10/17	6.8	35	3.2	R
25	Superstition Hill, California	1987/11/24	6.6	25	3	S
26	Edgecumbe, New Zealand	1987/03/02	6.4	15.5	2	N
28	Marryat, Australia	1986/03/03	5.8	13	0.005	R
29	Morgan Hill, California	1984/04/24	6.1	20	5.2	S
30	Borah Peak, Idaho	1983/10/28	6.9	36	0.15	N
31	Coalinga, California	1983/05/02	6.4	25	1.4	R
32	Sirch, Iran	1981/07/29	7.1	65	4.3	S
33	Corinth, Greece	1981/02/25	6.1	14	1.7	N
34	Corinth, Greece	1981/03/04	5.9	15	0.3	N
35	Daofu, China	1981/01/24	6.7	44	12	S
36	El Asnam (Ech Cheliff), Algeria	1980/10/10	6.9	36	0.8	R
37	Imperial Valley, California	1979/10/15	6.4	36	17	S
38	Coyote Lake, California	1979/08/06	5.8	14	11.9	S
40	Tabas, Iran	1978/09/16	7.4	90	1.3	R
41	Bob-Tangol, Iran	1977/12/19	5.8	19.5	4	S
42	Motagua, Nicaragua	1976/02/04	7.5	230	12	S
43	Luhuo, China	1973/02/06	7.5	90	14	S
44	San Fernando, California	1971/02/09	6.8	19	1.8	R
45	Tonghai, China	1970/01/04	7.2	60	2	S
46	Dasht-e-Bayaz, Iran	1968/08/31	7.1	80	5	S
47	Borrego Mtn, California	1968/04/09	6.6	33	6.7	S

*N, normal, S, strike slip, R, reverse.

this result include Allmann and Shearer (2009) and Baltay et al. (2011). Apparent exceptions have been reported based on Fourier spectra of smaller earthquakes, but as magnitude decreases, attenuation can cause spectral shapes to behave the same as they would for decreasing stress drop (e.g., Anderson, 1986). Studies that have taken considerable care to separate these effects have generally concluded that the average stress drop remains independent of magnitude down to extremely small magnitudes (e.g., Abercrombie, 1995; Ide et al., 2003; Baltay et al., 2010, 2011). However, all of these studies find that for any given fault dimension, the range of magnitudes can vary considerably (e.g., Kanamori and Allen, 1986). Despite this variability, it seems reasonable to evaluate a scaling relationship that is based on a constant stress

drop before considering the additional effect of the fault-slip rate. This vision guides the development of the considered scaling relationships. Details of these models for the relationship of stress drop and the fault dimensions are deferred to the Appendix. The following sections describe the data, present the summary equations for three alternative models, fit the alternative models to the data, and discuss the results.

Data

Tables 1 and 2 give the preferred estimates of M_w, L_E, and S_F for the earthquakes used in this analysis. These values and their corresponding uncertainty ranges are given in Table S1 (Ⓔ available in the electronic supplement to this
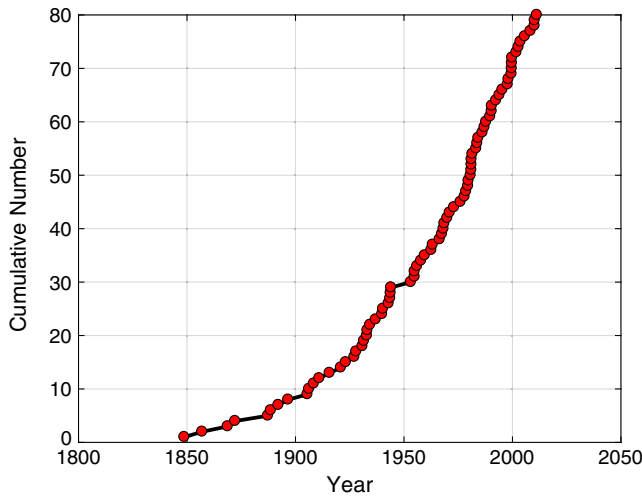
Table 2
Earthquakes from 1848–1967 Used in This Study

Event Number	Event Name	Event Date (yyyy/mm/dd)	M_w	Rupture Length (km)	Slip Rate (mm/yr)	Mechanism*
48	Mudurnu Valley, Turkey	1967/07/22	7.3	80	18	S
49	Parkfield, California	1966/06/28	6.2	28	30	S
51	Alake Lake or Tuosuohu Lake or Dulan, China	1963/04/19	7.0	40	12	S
52	Ipak or Buyin-Zara, Iran	1962/09/01	7.0	100	1	R
53	Hebgen Lake, Montana	1959/08/18	7.3	25	0.5	N
54	Gobi-Altai, Mongolia	1957/12/04	8.1	260	1	S
55	San Miguel, Mexico	1956/02/14	6.6	20	0.3	S
56	Fairview Peak, Nevada	1954/12/16	7.1	46	0.14	N
57	Dixie Valley, Nevada	1954/12/16	6.6	47	0.5	N
58	Yenice–Gonen, Turkey	1953/03/18	7.3	60	6.8	S
60	Gerede-Bolu, Turkey	1944/02/01	7.3	155	18	S
61	Tosya, Turkey	1943/11/26	7.6	275	19	S
62	Tottori, Japan	1943/09/10	6.9	33	0.3	S
63	Niksar-Erbaa, Turkey	1942/12/20	6.8	50	19	S
64	Imperial Valley, California	1940/05/19	7.1	60	17	S
65	Erzincan, Turkey	1939/12/25	7.8	330	19	S
66	Tuosuo Lake, Huashixia, China	1937/01/07	7.6	150	11	S
67	Parkfield, California	1934/06/08	6.2	25	30	S
68	Long Beach, California	1933/03/10	6.4	22	1.1	S
69	Changma, China	1932/12/25	7.6	149	5	S
70	Fuyun, China	1931/08/10	7.9	160	0.3	S
71	North Izu, Japan	1930/11/25	6.9	28	2.4	S
72	Laikipia, Kenya	1928/01/06	6.8	38	0.18	N
73	Tango, Japan	1927/03/07	7.0	35	0.3	S
74	Luoho-Qiajiao (Daofu), China	1923/03/24	7.3	80	10	S
75	Haiyuan, China	1920/12/16	8.0	237	7	S
76	Pleasant Valley, Nevada	1915/10/03	7.3	61	0.1	N
77	Chon-Kemin (Kebin), Kazakhstan	1911/01/03	8.0	177	2	R
78	San Francisco, California	1906/04/18	7.9	497	21	S
79	Bulnay, Mongolia	1905/07/23	8.5	375	3	S
80	Laguna Salada, Mexico	1892/02/23	7.2	42	2.5	S
81	Rikuu, Japan	1896/08/31	7.2	40	1	R
82	Nobi/Mino-Owari, Japan	1908/06/28	7.4	80	1.6	S
83	Canterbury, New Zealand	1888/09/01	7.1	65	14	S
84	Sonora, Mexico	1887/05/13	7.2	101.8	0.08	N
85	Owens Valley, California	1872/03/26	7.4	110	3.5	S
86	Hayward, California	1868/10/01	6.9	61	8	S
87	Fort Tejon, California	1857/01/09	7.8	339	25	S
88	Marlborough, New Zealand	1848/10/16	7.5	134	5.6	S

*N, normal, S, strike slip, R, reverse.

article), along with the references for all estimates. Events considered for analysis come from AWS96 and Biasi and Wesnousky (2016). Some AWS96 events were not used because uncertainties in one or more of the magnitude, length, or slip-rate parameters were considered too large or too poorly known to contribute to the parametric regressions. Events in Biasi and Wesnousky (2016) were selected on the basis of having a well-mapped surface rupture and non-geologically estimated magnitude. Their list builds on the list of fault ruptures of Wesnousky (2008) by adding more recent events and by including surface ruptures newly documented by geologic field work. Interested readers are referred to these previous papers for further description of each event. Overall, the database is heavily weighted toward surface-rupturing earthquakes. Some events in Biasi and Wesnousky (2016) were not included for lack of a resolved fault-slip rate,

or because their rupture lengths were too short. Events with $L_E < 15$ km were generally not included. The smallest preferred estimate of M_w is 5.7.

Earthquakes after 1900 were only included if some independent (nongeologic) means was available to estimate magnitude. Moment estimates from waveform modeling were preferred to body-wave magnitudes where both were available. The six earthquakes prior to 1900 are particularly well documented, as described in Ⓔ the electronic supplement. Because L_E is known for these events and the uncertainty in M_w introduced by uncertain depth of faulting is less than 0.1, the measured slip in these events controls M_w. It follows that estimating M_w from L_E alone for these events is not circular. The rupture length is normally taken as the distance between the ends of primary coseismic surface rupture. The sum of the lengths of overlapping traces may be

Figure 1. Cumulative number of events used in this analysis (Tables 1 and 2), shown as a function of time. The color version of this figure is available only in the electronic edition.


Figure 2. Event rates, as a function of magnitude and event types. The rates are estimated based on the approximation that the data represent about 100 yrs of seismicity, as discussed in the Data section. The color version of this figure is available only in the electronic edition.

used as the length in the analysis (e.g., event 53, Hegben Lake, 1959) where the overlapping portions were judged to contribute materially to the moment release. Rupture lengths based on aftershock distributions have generally been avoided, with the exception of six moderate strike-slip events, all in California. These were retained for continuity with AWS96 and for support of the regressions at moderate magnitudes. None control the results. Fault-slip rates are taken from offsets of geologic features 10–100 ka in age, where possible, to represent a stable recent slip-rate estimate. Fault-slip rates from paleoseismic offsets of one or a few individual earthquakes were avoided, because it is not clear how that activity would relate to the longer term average slip rate. Similarly, fault-slip rates from geodetic estimates were avoided where possible because they measure the current-day rate but may not represent the longer term average. Fault creep effects were considered, but no corrections were attempted in the database. First, creep is believed to affect only a few percent or less of events, and at a fraction of the full slip rate. Second, uncertainty in fault-slip rate will be seen below to have little effect on the regression.

Figure 1 shows the cumulative number of earthquakes used as a function of time. From 1954 to 2013, the rate of usable events is relatively steady, about 0.9 events per year. The rate is lower prior to ~1954 suggesting that the earlier historical record is less complete.

The earthquakes are separated into general categories of strike-slip, normal, and reverse faulting. Figure 2 shows the exceedance rates of considered earthquakes in each of these categories as a function of magnitude, both combined and separated by focal mechanism. To estimate the rates, the number of earthquakes for each of the curves was divided by 100 yrs. This is obviously an approximation, but considering Figure 1, the events prior to ~1910 may roughly compensate for the missing events since 1910. For instance, Figure 2 suggests that continental events that cause surface rupture with
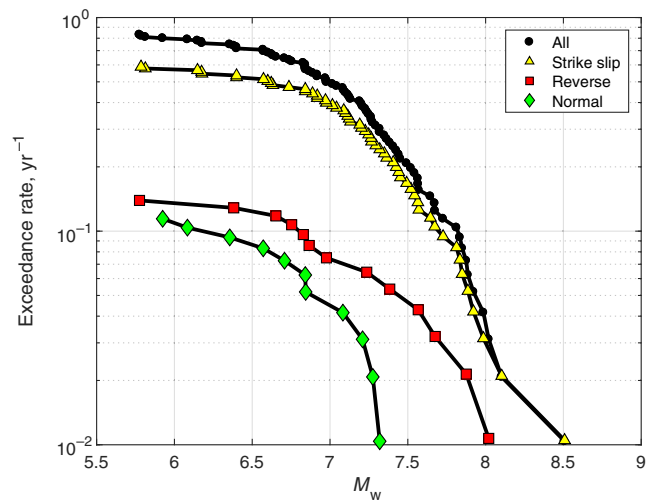
$M_w \geq 7.0$ have occurred at a rate of about 0.5 yr^{-1}, or roughly once every two years. The rates of strike-slip, reverse, and normal mechanisms are about 0.4, 0.075, and 0.045 yr^{-1}. Rounded to the nearest 5%, this implies that about 75% of those events were strike slip, about 15% had reverse mechanisms, and about 10% had normal mechanisms.

Figure 3 shows maps with locations of all events, using different symbols to distinguish among mechanisms. The insets show more details on locations of events from the western United States, the eastern Mediterranean region, and Japan.

Figure 4 plots the preferred slip rates versus the preferred rupture lengths. Figure 4a emphasizes the overall distribution of the data, while 4b highlights the 56 strike-slip faults, 4c highlights the 13 reverse faults, and 4d highlights the 11 normal faults. The combined data in Figure 4a are distinctly upper triangular. The points along the diagonal associate an increase in fault length with an increase in fault-slip rate, which in turn is likely a function of cumulative slip (e.g., Wesnousky, 1988, 1999) that does not depend on the mechanism. The data above the diagonal show that (1) the entirety of long faults and fault systems does not always break and that (2) small fast faults may exist. There are two alternatives to explain the lack of long ruptures on faults with low slip rates. The first could be purely statistical because events in the lower right corner of the plot could be too rare to be represented in the historical record. Alternatively, due to what Perrin et al. (2016) call "the competition between damage and healing processes," faults with slow slip rates might, during the interseismic period, be sufficiently affected by differential healing, influences from adjacent faults, or other processes that long ruptures on slow faults never occur.

Figure 4b–d emphasizes the data available to search for slip-rate dependency for the three fault types. Figure 4b
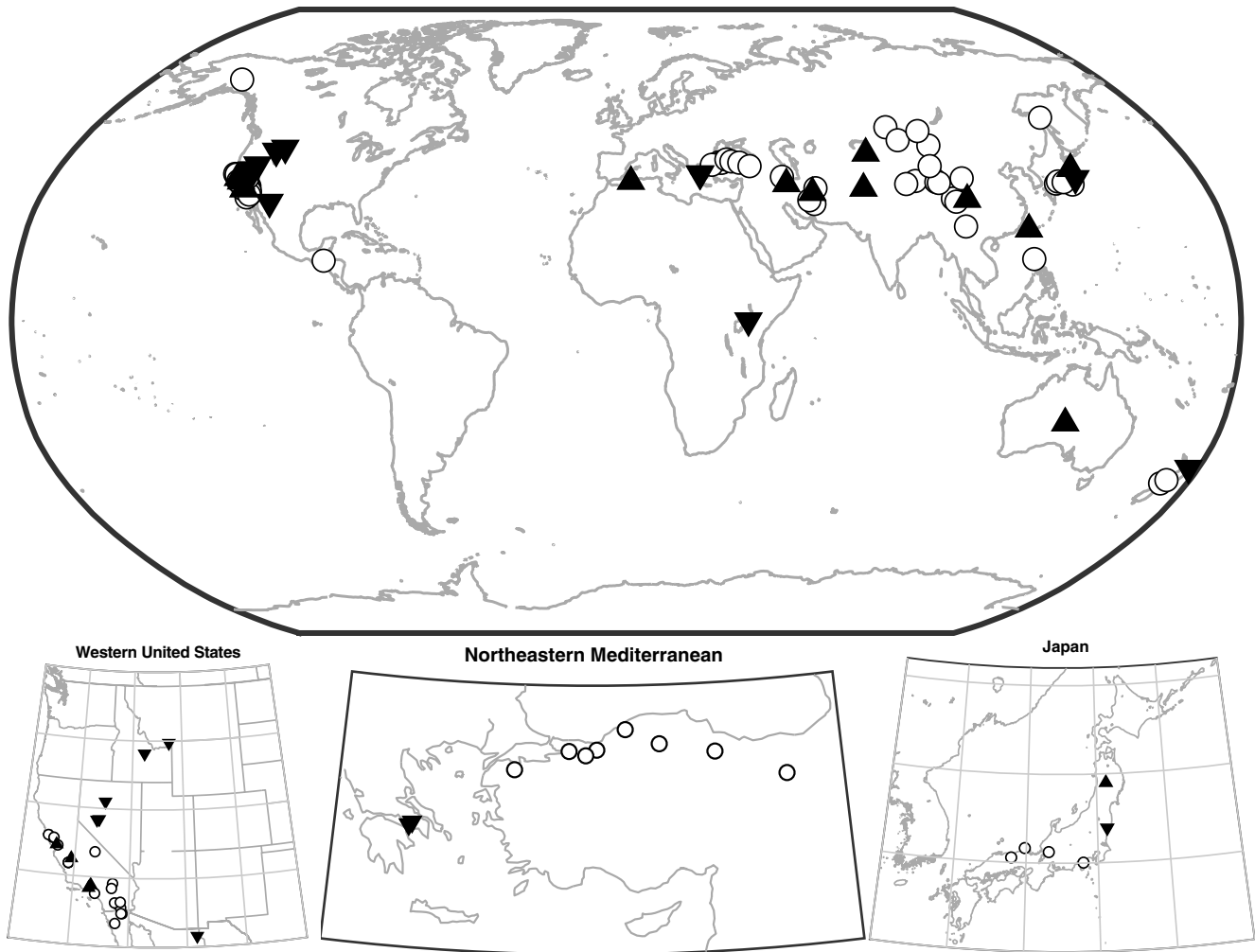
Figure 3. Locations of events considered in this study. Open circles show locations of events with a strike-slip mechanism. Triangles represent reverse events, and inverted triangles represent normal mechanisms.

shows a distribution of points spanning rupture lengths mostly between 20 and 400 km and slip rates between 0.3 and 30 mm/yr. Rupture lengths for reverse faults (Fig. 4c) range from 13 to 240 km although most are between 20 and 100 km. Slip rates for reverse faults are mostly between 0.4 and 4 mm/yr, with outliers at 0.005 and 12.9 mm/yr. Rupture lengths and slip rates for normal faults (Fig. 4d) range from 14 to 102 km and 0.08 to 2 mm/yr, but are unevenly distributed within these limits.

Modeling Approaches

The effect of slip rate is tested against three model shapes for the scaling relationship to confirm that it is not an artifact of a particular assumption for how magnitude depends on rupture length. The first M1 explores a linear regression of M_w with the logs of length and slip rate:

$$M_w = c_0 + c_1 \log L_E + c_2 \log \frac{S_F}{S_0}, \qquad (1)$$

in which L_E is the rupture length (measured along strike) of a specific earthquake; M_w is the reported moment magnitude for the respective earthquake (Kanamori, 1977); S_F is the slip rate of the fault on which the earthquake occurred determined from geological observation; S_0 is the average of the logs of all slip rates in the data set being considered (e.g., strike-slip faults, normal faults, etc.); and c_0, c_1, and c_2 are coefficients of regression to be determined. Mathematically, c_0 trades off with $-c_2 \log S_0$, which allows the parameter S_0 to be rounded to two significant digits. In this model, setting $S_F = S_0$ is mathematically equivalent to setting $c_2 = 0$ and thus also equivalent to the model approach used by Wells and Coppersmith (1994) and others who estimate a linear dependence of M_w on $\log L_E$ without including the slip rate on the fault. Two misfit parameters are considered. The first σ_{1L} is the standard deviation of the difference between observed and predicted magnitudes when $c_2 = 0$, so only L_E is used to estimate M_w, while σ_{1S} is the corresponding standard deviation when the slip-rate term in equation (1) is incorporated. A consequence of the assumed model M1 is
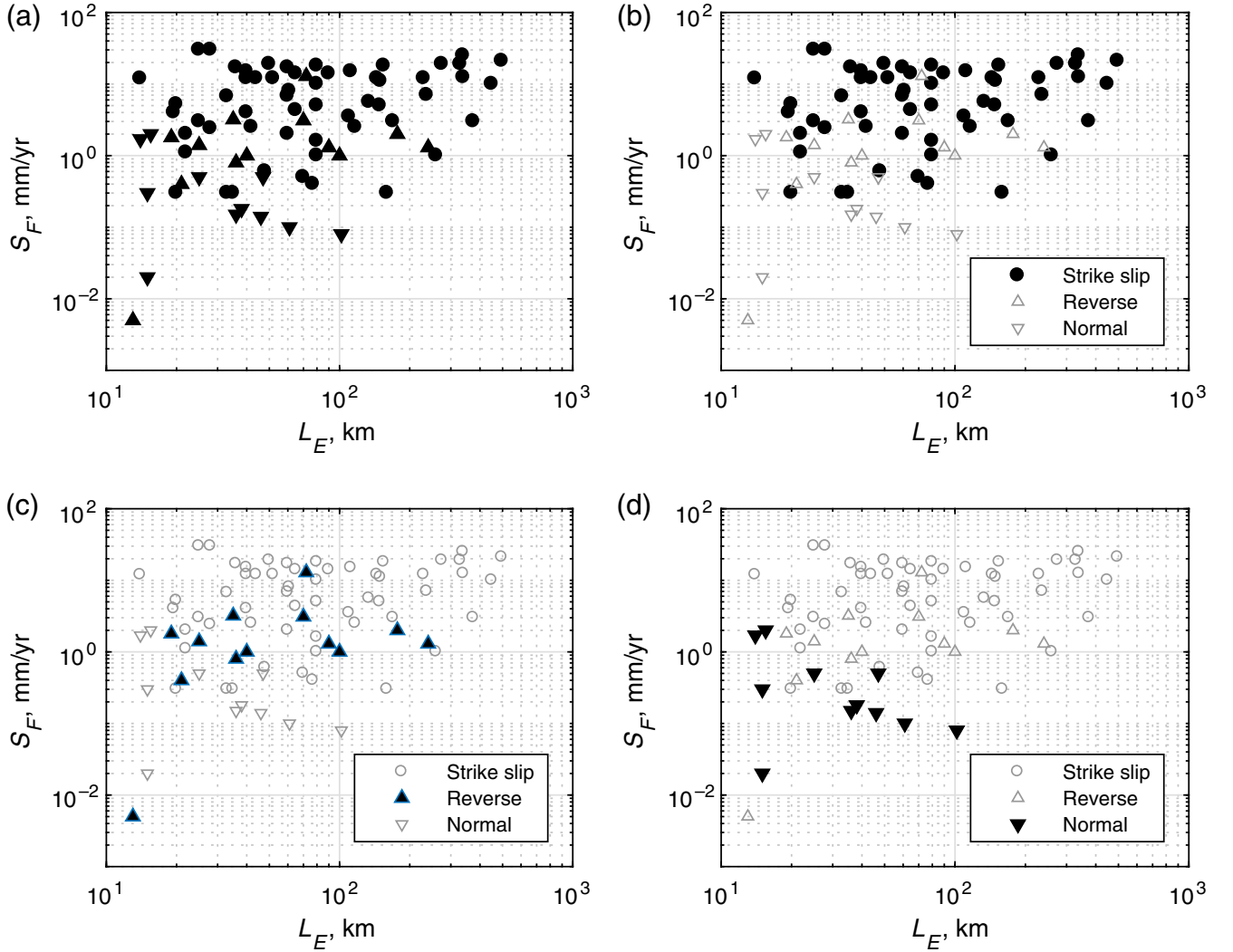
Figure 4.   Rupture length–slip-rate distribution of the data in Tables 1 and 2. All points are shown combined in each part of the figure, (a) each fault type is given equal emphasis, (b) strike-slip faults are emphasized, (c) reverse faults are emphasized, and (d) normal faults are emphasized. The color version of this figure is available only in the electronic edition.

that unless c_1 fortuitously equals 2/3, stress drop increases for large earthquakes as a function of rupture length L_E, regardless of whether slip rate is included or not (Table A1).

The second M2 constrains the slope to give constant stress drop for small and large earthquakes with a slope change at the break-point magnitude M_{bp}. The stress drop for small and large earthquakes is allowed to differ:

$$M_w = \begin{cases} M_{bp} + c_{1C} \log\left(\frac{L_E}{L_{bp}}\right) + c_2 \log\left(\frac{S_F}{S_0}\right) & L_E < L_{bp} \\ M_{bp} + c_{1L} \log\left(\frac{L_E}{L_{bp}}\right) + c_2 \log\left(\frac{S_F}{S_0}\right) & L_E \geq L_{bp}, \end{cases} \quad (2)$$

in which $c_{1C} = 2$ and $c_{1L} = 2/3$ for rupture lengths that are less than or greater than L_{bp}, respectively, the rupture length where slope changes from 2 to 2/3. The three unknown parameters in model M2 are L_{bp} the rupture length where the slope changes from 2 to 2/3, M_{bp} the magnitude at that transition, and c_2 which is again the sensitivity of magnitude to fault-slip rate. Ruptures of length less than L_{bp} are considered to be a small earthquake and scale like a circular rupture in Table A1, implying that constant stress drop occurs when $c_{1C} = 2$. An earthquake with rupture length greater than L_{bp} is considered to be a large earthquake and corresponds to one of the models for a long fault in Table A1 (depending on fault mechanism), for which the value $c_{1L} = 2/3$ results in constant stress drop. However, equation (2) does not require the stress drop for the small earthquakes to be the same as the stress drop for large earthquakes. Equation (2) has the same number of unknown parameters to be determined from the data as equation (1). The two standard deviations of the misfit for model M2 are σ_{2L} and σ_{2S}, which correspond directly to the parameters σ_{1L} and σ_{1S} of model M1.

The third model M3 is derived from the model of Chinnery (1964) for a vertical strike-slip fault that ruptures the surface. It is assumed that stress drop for the top center of the fault in this model $\Delta\tau_C$ is constant across all rupture lengths and magnitudes:

$$M_{\mathrm{w}} = \begin{cases} 2\log L_E + \frac{2}{3}\log \Delta\tau_C + \frac{2}{3}\left(\log \frac{2\pi}{C_{LW}^2 C(\gamma)} - 16.1\right) + c_2 \log\left(\frac{S_F}{S_0}\right) & \frac{L_E}{C_{LW}} < W_{\max} \\[2ex] \frac{2}{3}\log L_E + \frac{2}{3}\log \Delta\tau_C + \frac{2}{3}\left(\log \frac{2\pi W_{\max}^2}{C(\gamma)} - 16.1\right) + c_2 \log\left(\frac{S_F}{S_0}\right) & \frac{L_E}{C_{LW}} \geq W_{\max}, \end{cases} \tag{3}$$

in which

$$C(\gamma) = 2\cos\gamma + 3\tan\gamma - \frac{\cos\gamma \sin\gamma (3 + 4\sin\gamma)}{(1 + \sin\gamma)^2}. \tag{4}$$

Details on the development of the model M3 equations are provided in the Appendix. The value γ is the angle from the top center of the fault to either of the bottom corners, that is, $\tan\gamma = 2W_E/L_E$, in which W_E is the down-dip width of the earthquake rupture. The model variables include four parameters. These are the aspect ratio of the fault for small ruptures $C_{LW} = L_E/W_E$, the stress drop $\Delta\tau_C$, the coefficient that quantifies the slip-rate dependence c_2, and the maximum fault width $W_{\max}$. Equation (3) assumes that the aspect ratio is constant for small earthquakes and that when the selected aspect ratio in combination with L_E implies a width greater than $W_{\max}$ the width is set to $W_{\max}$. For model M3, the two standard deviations of the misfit are σ_{3L} and σ_{3S}, corresponding to the parameters σ_{1L} and σ_{1S} of model M1. As written, the coefficients of the term in $\log L_E$ appear to be the same as in model M2, but for the long ruptures, γ depends on L_E, so the term with $C(\gamma)$ modifies the slope.

Model equations (1)–(3) require different strategies to obtain their unknown coefficients. The simplest way to find the unknown coefficients for equation (1) is using a linear least-squares regression, which minimizes the misfit of the prediction of M_{w} but does not account for uncertainties in L_E or S_F. AWS96 approached this difficulty by carrying out multiple regressions for points chosen at random within the range of allowed values of all three parameters, and then looked at the distribution of derived values of the coefficients of the regression. Alternative approaches to find the coefficients, described variously as "total least squares" or "general orthogonal regression" (e.g., Castellaro *et al.*, 2006; Castellaro and Bormann, 2007; Wikipedia article "Total Least Squares," see Data and Resources) were also considered for this analysis. The approach by AWS96 turned out to give the least biased results for a set of synthetic data with an uncertainty model that we considered to be realistic and consistent with the actual data, so their approach is also used in this study. The parameters for equation (1) were determined from 10,000 realizations of the randomized earthquake parameters to find the distributions of coefficients.

In implementing the AWS96 approach, M_{w}, L_E, and S_F are chosen at random from the range of uncertainties given in Ⓔ the electronic supplement. The probability distributions for the randomized parameters reflect that uncertainty ranges are not symmetrical around the preferred value. The preferred value is set to be the median. As an example, the probability distribution for the ith randomized value of L_E is as follows:

$$p(L_E) = \begin{cases} \frac{1}{(L_E^{\mathrm{pref}} - L_E^{\min})} & (\text{case A}) \\[1.5ex] \frac{1}{(L_E^{\max} - L_E^{\mathrm{pref}})} & (\text{case B}), \end{cases} \tag{5}$$

in which case A has probability of 0.5, case B has probability of 0.5, $L_E^{\min}$ and $L_E^{\max}$ are the minimum and maximum of the range on the rupture length, respectively, and L_E^{pref} is the preferred value. The seismic moment and slip rate are randomized using the same algorithm, and M_{w} is found from the randomized moment. The standard deviations of the misfit σ_{1L} and σ_{1S} are the average values from the multiple realizations.

Equation 2 has the additional complication of being nonlinear in L_{bp}. We approach the solution by reorganizing equation (2) as

$$M_{\mathrm{bp}} + c_2 \log\left(\frac{S_F}{S_0}\right) = M_{\mathrm{w}} - c_{1x}\log\left(\frac{L_E}{L_{\mathrm{bp}}}\right), \tag{6}$$

in which c_{1x} is either c_{1C} or c_{1L} depending on L_E. Assuming a value for L_{bp}, it is straightforward to find the unknown coefficients M_{bp} and c_2. We considered a set of closely spaced values of L_{bp} from the smallest to the longest rupture length in the data, and choose the value with the smallest total misfit. For each trial value of L_{bp}, we solved for the unknown coefficients 10,000 times with values of M_{w}, L_E, and S_F randomized as in equation (5), and our preferred model is the mean of the coefficients from the multiple realizations.

Model M3 (equation 3) has four unknown parameters, in which the effects of C_{LW} and $W_{\max}$ are nonlinear (Fig. A1). For this reason, a grid of values of C_{LW} and $W_{\max}$ was searched; there were 506 points on this grid. For each grid point, $\Delta\tau_C$ and c_2 were determined by linear least squares for 10,000 randomly chosen realizations of M_{w}, L_E, and S_F. The average values of $\Delta\tau_C$ and c_2 were found from the distributions of these realizations, together with the average values of σ_{3L} and σ_{3S}. This permitted creating a contour plots of σ_{3L} and σ_{3S} as a function of the trial values of C_{LW} and $W_{\max}$. The minima in σ_{3L} and σ_{3S} did not generally occur for the same combinations of C_{LW} and $W_{\max}$. Because the results of model M3 might potentially be used for faults where slip rate is unknown, we minimized σ_{3L}. The minimum in σ_{3L} is broad compared with the grid spacing of C_{LW} and $W_{\max}$, so the values that are used come as near as possible, within the minimum of σ_{3L}, to minimize σ_{3S} as well. The grid limits considered the maximum fault widths from 10 to 20 km for strike-slip faults, whereas for reverse and normal faulting the grid limits considered the maximum fault widths from 18 to 30 km. The larger widths were considered because of the suggestions of King and Wesnousky (2007), Hillers and Wesnousky (2008), and Jiang and Lapusta (2016) that a dynamic rupture in a large earthquake might reasonably extend
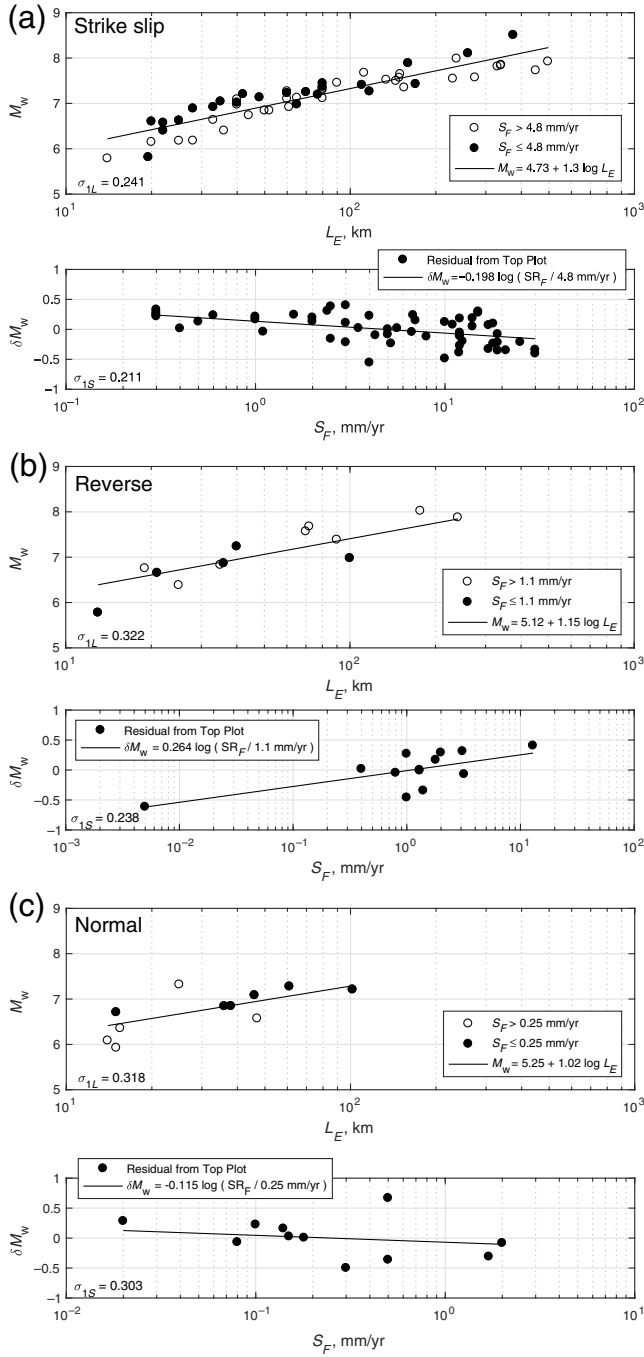
Figure 5. Model M1 (equation 1) for (a) strike-slip, (b) reverse, and (c) normal faults. For each mechanism, the upper frame shows M_w plotted as a function of L_E. Points are all the preferred values, as given in Tables 1 and 2. Solid points represent low slip-rate faults. The solid line uses coefficients given in Table 3 for $S_F = S_0$. The lower frame shows the residuals δM_w of the points in the upper frame from the solid line. The line in the lower frame shows the predicted effect of S_F based on the coefficients in Table 3, that is, $\delta M_w = c_2 \log(S_F/S_0)$. For strike-slip faults, the significant effect of fault-slip rate is seen in the clear separation of low and high slip-rate faults in the upper panel, and the negative slope of the fit to the residuals in the lower panel. For reverse and normal faults, the sparse data suggest a different trend in the residuals, indicating that mixing the three mechanism types is not appropriate.
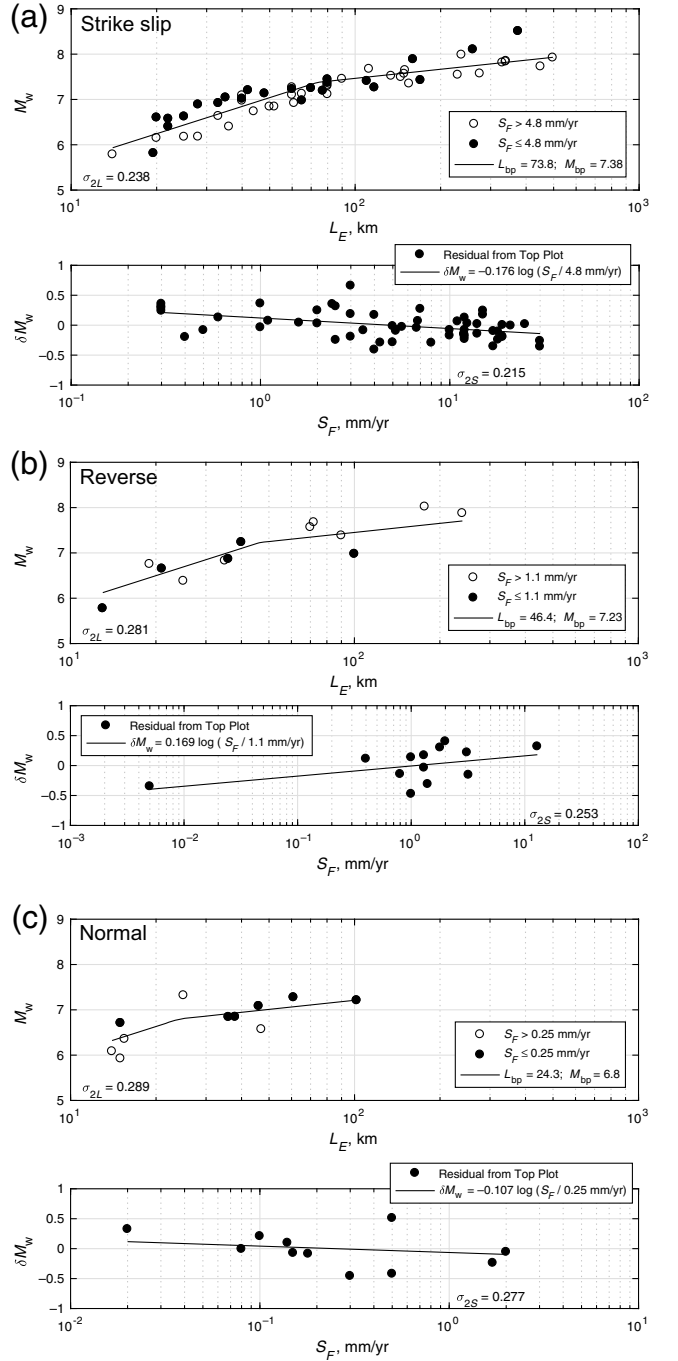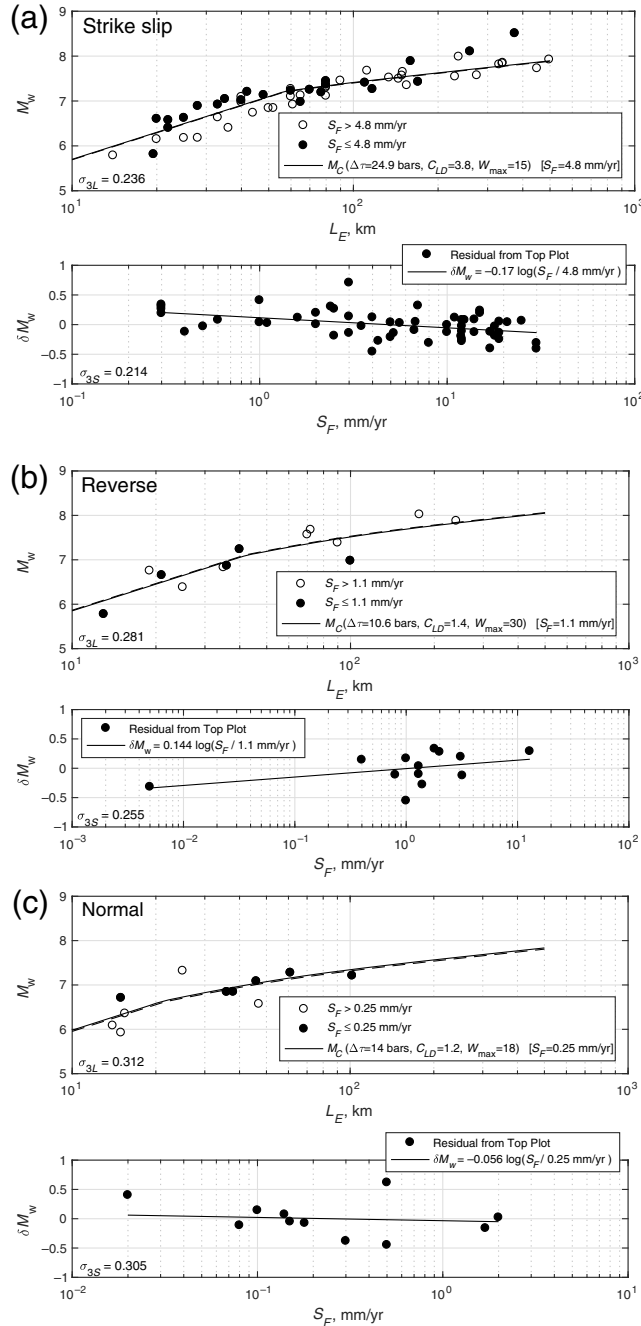
Figure 6. Model M2 (equation 2) for (a) strike-slip, (b) reverse, and (c) normal faults. Coefficients for the lines are given in Table 4. Other figure details are the same as in Figure 5.

deeper than the brittle crustal depths associated with microearthquakes.

Analysis Results

Figures 5–7 show results for models M1–M3, respectively, for strike-slip, reverse-, and normal-faulting earthquakes. For each mechanism, the curve in the upper frame shows predicted values of magnitude $\hat{M}_w$ for $S_F = S_0$. The

Figure 7. Model M3 (equation 3) for (a) strike-slip, (b) reverse, and (c) normal faults. Coefficients for the lines are given in Table 5. Other figure details are the same as in Figure 5.
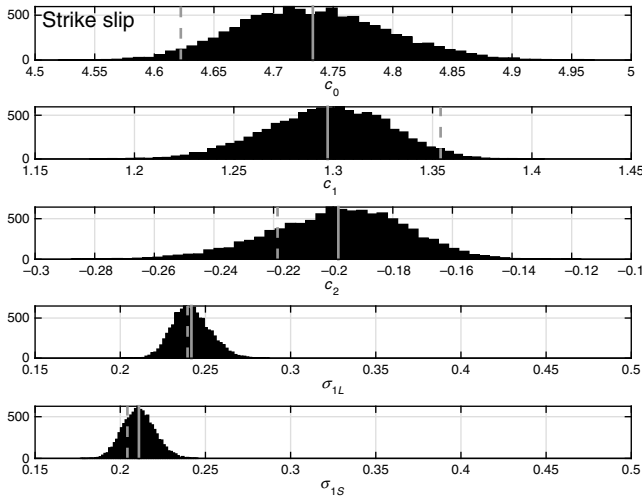
Table 3
Coefficients for Model M1, Use in Equation (1), the Different Fault Types Considered Separately, and Earthquakes Listed in Tables 1 and 2

Parameter	Strike Slip	Reverse	Normal
c_0	4.73 ± 0.062	5.12 ± 0.11	5.25 ± 0.18
c_1	1.30 ± 0.031	1.15 ± 0.065	1.02 ± 0.12
c_2	-0.198 ± 0.023	0.264 ± 0.036	-0.115 ± 0.109
S_0 (mm/yr)	4.8	1.1	0.25
σ_{1L}	0.241	0.322	0.318
σ_{1S}	0.211	0.238	0.303

Table 4
Coefficients for Model M2, Use in Equation (2), the Different Fault Types Considered Separately, and Earthquakes Listed in Tables 1 and 2

Parameter	Strike Slip	Reverse	Normal
L_{bp}	73.8 ± 9.4	46.4 ± 6.4	24.3 ± 1.10
M_{bp}	7.38 ± 0.070	7.23 ± 0.091	6.80 ± 0.031
c_2	-0.176 ± 0.031	0.169 ± 0.042	-0.107 ± 0.091
S_0 (mm/yr)	4.80	1.1	0.25
σ_{2L}	0.238	0.281	0.289
σ_{2S}	0.215	0.253	0.277

Model M1: The Linear Model

The parameters for the linear models are given in Table 3. Figure 8 shows the distribution of coefficients found for 10,000 trials for strike-slip faults. The widths of these distributions are used to estimate the uncertainty in each coefficient. The coefficients c_0, c_1, and c_2 are found simultaneously, as opposed to a possible alternative approach, in which c_0 and c_1 could be found first, and then c_2 is determined by a second independent linear fit to the residuals. For strike-slip events, which dominate the data, $c_2 = -0.198 \pm 0.023$ (Fig. 5a) so δM_w is observed to be a decreasing function of slip rate, similar to AWS96. The data with a reverse mechanism support δM_w increasing, rather than decreasing, with increased slip rate (Fig. 5b), whereas for the events with a normal mechanism the slip-rate dependence of δM_w is not distinguishable from zero (Fig. 5c). Considering the distribution of slip-rate data for reverse faults in Figure 5b, it may be observed that the finding of slip-rate dependence is the result of mainly a single outlier, the Marryat earthquake (M_w 5.8, event number 28 in Table 1) which is reported to have a slip rate of 0.005 mm/yr. Intracontinental events are included considering, based on Byerlys law, that the physics of rupture of crystalline rocks within the range of typical crustal compositions is not, *a priori*, different merely because the fault is located far from a plate boundary or that rock type might be different (e.g., Byerlee, 1978; Scholz, 2002). Also, the Marryat Creek event tends to decrease the slip-rate dependence of δM_w, as a consideration of the remaining points would reveal.

lower frame shows the residuals from this prediction, defined as

$$\delta M_{wi} = M_{wi} - \hat{M}_{wi}, \qquad (7)$$

for each considered earthquake, and the solid line is given by $\delta M_w = c_2 \log(S_F/S_0)$. Model coefficients and uncertainties in estimates of M_w for models M1–M3 are given in Tables 3–5, respectively.

Figure 8. Coefficient distributions for the linear strike-slip model (M1, equation 1). The bar chart shows number of occurrences of parameter values among 10,000 realizations for randomly selected values of M_w, L_E, and S_F within the uncertainty range of each. The solid gray line shows the mean value of each parameter. The dashed gray line shows the value found for the preferred value of M_w, L_E, and S_F for each earthquake. The clear negative value of c_2 corresponds to decreasing relative magnitude predictions with increasing slip rate.

Nonetheless, the positive slope of δM_w in Figure 5b for reverse faulting is not a robust result.

Considering Figure 5, the results for the linear model provide an indication that it is not appropriate to combine different fault mechanisms in this type of regressions. The AWS96 model from all rupture mechanisms was $M_w = 5.12 + 1.16 \log L_E - 0.20 \log S_F$, which is only slightly different from the strike-slip case in Figure 5a. That result is consistent with the AWS96 model being dominated by strike-slip earthquakes, and thus demonstrates continuity with the previous study. However, results here separated by mechanism indicate that the slip-rate dependence in AWS96 is controlled by the behavior of strike-slip earthquakes, and not much affected by the normal mechanisms that show little or no slip-rate dependence, and the reverse mechanisms that potentially show a different dependence. Suppose as a thought experiment that the dip-slip cases have no slip-rate dependence, or in other words, that the variability with slip rate is pure noise. A strong

strike-slip case plus some noise will still resolve to a decently significant trend even though we added only noise. In applying the combined regression to dip-slip faults, we may be projecting back from the strong case into the noise, and saying things about future dip-slip earthquake expectations that are not likely based on the available data.

Model M2: The Bilinear Model

Table 4 gives estimated coefficients for model M2 (equation 2), and Figure 6 illustrates the fit to the data. Without the slip-rate adjustment, the bilinear model fits the observed magnitudes as well or better than the linear model M1, as shown by similar or smaller values of σ_{2L} than the corresponding values of σ_{1L}. The results again show a dependence of magnitude on slip rate for strike-slip faults (Fig. 6a) but not dip-slip faults (Fig. 6b,c). The value of σ_{2S} is comparable to σ_{1S} for the strike-slip case but larger for the dip-slip faults. For the strike-slip case, the fit to the data in Figure 6a is better at large rupture lengths than in Figure 5a.

Model M3: The Constant Stress-Drop Model

Parameters for model M3 are given in Table 5, and the fit to the data is illustrated in Figure 7. Some features of Figure 7 are noteworthy. For the strike-slip case, the points for faults with low slip rates (solid points) are mostly above the average model, whereas points with high slip rates (open circles) are mostly below the average. This slip-rate dependence is reinforced in the lower frame of Figure 7a, where the slope of the linear fit to the residuals is more than five standard deviations of the slope different from zero. The variance reduction by the addition of the slip-rate term is statistically significant with 80% confidence, based on the F-test. The same remarks apply for models M1 (Fig. 5) and M2 (Fig. 6).

The strike-slip case in Figure 7a uses $W_{max} = 15$ km, whereas Table 5 gives model M3 parameters for $W_{max} = 20$ km as well. The data do not prefer either of these two models, as the curves and the misfits characterized by σ_{3L} and σ_{3S} are barely distinguishable, so the plot for the $W_{max} = 20$ km model is not shown. For the 20 km wide strike-slip case, both σ_{3L} and σ_{3S} are smaller than the equivalent uncertainties in models M1 or M2. Although this improvement is small and statistically insignificant, it is encouraging that a model with constant stress drop achieves this result. Hanks and Bakun (2014) discussed the difficulties associated with several scaling models for long strike-slip faults, which fit the longest earthquakes either by increasing the rupture width by penetrating into the crust below the depths of microearthquakes or by increasing the stress drop. Although Hanks and Bakun (2014) consider the deep penetration of strike-slip faults below the depth of microearthquakes to be unlikely, we provide both models. Recent

Table 5
Coefficients for Model M3, Use in Equation (3), the Different Fault Types Considered Separately, and Earthquakes Listed in Tables 1 and 2

Parameter	Strike Slip (15 km)	Strike Slip (20 km)	Reverse	Normal
$\Delta\tau_C$ (bars)	24.9 ± 1.1	15.3 ± 0.7	10.6 ± 0.7	14.0 ± 1.5
C_{LW}	3.8	2.9	1.4	1.2
W_{max} (km)	15	20	30	18
c_2	-0.170 ± 0.029	-0.174 ± 0.029	0.144 ± 0.027	-0.056 ± 0.095
S_0 (mm/yr)	4.8	4.8	1.1	0.25
σ_{3L}	0.236	0.235	0.281	0.312
σ_{3S}	0.214	0.210	0.255	0.305
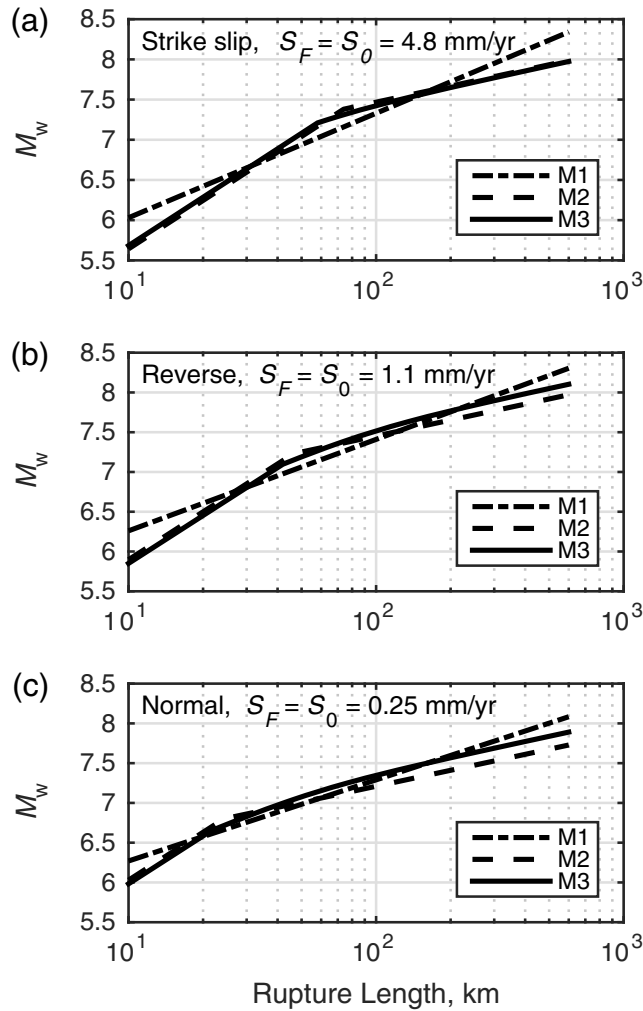
Figure 9. Comparisons of models M1, M2, and M3 for (a) strike-slip, (b) reverse, and (c) normal faults, using $S_F = S_0$ for each mechanism.

studies that favor deep penetration include Graves and Pitarka (2015) based on experience in modeling ground motions near the fault and Jiang and Lapusta (2016) based on the seismic quiescence of the ruptures of past large earthquake such as the 1857 earthquake on the San Andreas fault.

The ability to model the data using equation (3) unfortunately does not resolve the "no high stress drop/no deep slip enigma" articulated by Hanks and Bakun (2014), but rather pushes it into issues with the aspect ratio and the absolute value of the constant stress drop. The $W_{max} = 15$ km model uses a large aspect ratio of $C_{LW} = 3.8$, compared with $C_{LW} = 2.9$ for the $W_{max} = 20$ km model, or 2.4 at the transition to fix the width of 15 km in the Hanks and Bakun (2014) model. The higher aspect ratio for the $W_{max} = 15$ km model would also imply that earthquakes such as the M_w 6.6 Superstition Hills event (number 25) or the M_w 6.2 Parkfield 1966 event (number 49) only penetrate from the surface to about 7 km depth. Also, the stress drop for the $W_{max} = 15$ km model is rather high, $\Delta\tau_C \approx 25$ bars, considering that

this corresponds to $\Delta\tau_S \approx 50$ bars (see the Appendix) in the more frequently used model of Kanamori and Anderson (1975). We suggest that variability of the aspect ratio must contribute to the uncertainties in these scaling relations at the lower magnitudes.

For the reverse-faulting data, we considered values of W_{max} up to 30 km because reverse faults can have low dips, and that upper limit is the preferred value. For normal faulting, we only considered the values of $W_{max} > 18$ km, because constrained observations of normal faults imply that the fault width can be that wide (e.g., Richins *et al.*, 1987). For model M3 to fit the sparse normal-faulting data as well as model M2, we would need to use a much smaller value of W_{max}.

Comparisons

Figure 9 compares the models for the three different types of mechanisms. Models M2 and M3 tend to resemble each other most closely, whereas model M1, being linear, tends to give larger magnitudes for long and short faults but smaller magnitudes in the center of the length range.

Discussion

The larger data set modeled here compared with AWS96 expands our understanding of slip-rate dependence for the scaling of magnitude and rupture length. Improvements in estimates of the magnitudes of earthquakes are realized with slip-rate dependence for strike-slip faults for all three models considered here. Thus, the slip-rate dependence in this case is not an artifact of the underlying scaling model. The distribution of data in $L_E - S_F$ space (Fig. 4b) gives further reason for confidence in the strike-slip case. On the other hand, individual models for reverse and normal faulting have, at best, an equivocal place for slip-rate dependence. This again is consistent with the uneven distribution of data on the plots of $L_E - S_F$ in Figure 4c,d. For models M1 and M2 of the normal-faulting events, but not for model M3, the sign of slip-rate dependence agrees with the strike-slip case. Thus, normal faulting could have slip-rate dependence nudging estimates toward smaller magnitudes for higher slip-rate faults but lacks sufficient data to prove it. The reverse-faulting events disagree even at the sign of the effect. The disagreement is present whether we retain either or both of the apparent outliers in Figures 5–7. Thus, based on the current data, we do not find support for the general reduction of magnitude with slip rate implied by the combined set regression of ASW96. It appears that the strength of the slip-rate effect among strike-slip events and their sheer numbers relative to dip-slip events overwhelm the ambiguous (normal) and contrary (reverse) data, leading to an apparently general slip-rate relationship among all data. Thus, our new data set contributes to the understanding that slip-rate dependence is dominantly a strike-slip fault effect that is not inconsistent with normal faulting, and not apparently consistent with reverse

mechanism fault rupture. The data available to AWS96 did not permit this distinction.

If we are guided by studies of earthquake source physics, model M3 may be preferable to models M1 or M2. Specifically, the advantage would be the constant stress drop of earthquakes over the full range of magnitudes, consistent with, for example, Allmann and Shearer (2009). The slope of the linear model M1 with rupture length implies that stress drop increases significantly with rupture length for large earthquakes. The slopes of the bilinear model M2 are consistent with simple models for scaling with constant stress drop in the small and large earthquake domains, but the stress drops in the two domains are different. In addition, because the buried circular rupture model by construction does not reach the surface, its applicability to the short ruptures of model M2 is not obvious.

Constant stress-drop model M3 has the important advantage compared with dislocation models in an unbounded space in that it is explicitly designed for surface-rupturing earthquakes. For this reason, we might expect that it will perform well where magnitude scaling is required for calculation of synthetic ground motions (e.g., Goulet *et al.*, 2015). The Chinnery (1964) model has uniform slip with a singularity of stress drop near its edges, which enables a closed-form solution. Stress drop in actual earthquakes is a variable function of location on the fault, so single values are always averages. The Chinnery (1964) approach is probably as reasonable as others. The application of the same functional form for dip-slip earthquakes is entirely *ad hoc*, of course. Although it is more complicated, its consistency with a physical model with a constant stress drop commends it as a preferred regression. Compared with the better-known equations summarized by Kanamori and Anderson (1975), the stress-drop parameter in this model is smaller, emphasizing that average stress-drop estimates are model dependent.

The adjustment that decreases magnitude for high-slip-rate strike-slip faults implies that the stress drop on those faults is lower than on faults of the same length with lower slip rate. The finding is consistent with the observations of Kanamori and Allen (1986) and Scholz *et al.* (1986) that a longer healing time results in a larger stress required to initiate rupture and thus a higher stress drop. For normal or reverse faulting, the slip-rate dependence is low, and the slip-rate coefficient c_2 is indistinguishable from zero. The findings suggest that, if c_2 is not zero for these cases, then c_2 is positive for reverse-faulting earthquakes. This is contrary to the hypothesis of Kanamori and Allen (1986). We suggest that if this positive slope is confirmed with added data, the physical mechanism may be related to the dynamics of rupture. For a reverse fault, the dynamic stresses on a rupture propagating up-dip are tensile as rupture approaches the surface, so the coefficient of friction or cohesion on the fault is less relevant.

There are a number of future studies that should be performed to improve upon the results presented here. The first is to examine the consistency of the models, and especially

model M3, with the observed fault displacement. If the results, based on the definition of seismic moment (equation A2), agree with seismic data, the scaling relationship presented here would be an alternative to the self-consistent scaling model of Leonard (2010, 2014) for earthquakes in continental crust.

The second issue that deserves attention is handling multisegment faults. We consider, for instance, the 1905 Bulnay, Mongolia, earthquake, which is the strike-slip point in Figures 5–7 at 375 km and M_w 8.5. The 375 km length is the distance from one end of the rupture to the other, and does not include a spur fault in between that is 100 km long. This event points out that the standard deviations σ_{xL} and σ_{xS} for all three models include the potential presence of spur or sub-parallel faults that do not increase the total end-to-end length of the rupture. Several other faults in Tables 1 and 2 have similar issues. A better understanding of how seismic moment is distributed on multiple segments and fault splays, as well as how best to measure the lengths of multiple segment ruptures and how to recognize these features ahead of the earthquake would help to reduce uncertainties in future studies of scaling relations. If the result is different from the approach used by Uniform California earthquake rupture forecast, v. 3 (UCERF3), it could have a direct impact on future seismic-hazard analyses.

Conclusions

The primary question asked by this research is if the introduction of slip rate on a fault helps to reduce the uncertainties in estimates of magnitude from observations of rupture length. We find that such a slip-rate dependence is reasonably well established for strike-slip cases: as the slip rate increases for any given fault length, the predicted magnitude tends to decrease. This result is robust in the sense that the slope of the residuals with slip rate is significantly different from zero, and the variance reduction is modestly significant for all three of the considered models relating rupture length and magnitude. For reverse- and normal-faulting mechanisms, on the other hand, our data do not demonstrate the presence of a significant slip-rate effect in the relationship between rupture length and magnitude. Compared with original results in AWS96, we now suggest slip rate be included only for strike-slip faults.

The constant stress-drop model presented here has potential for progress on a standing difficulty in ground-motion modeling of an internally consistent scaling of magnitude, length, down-dip width, and fault displacement. Current relations in which magnitude scales with length or area lead to unphysical stress drops or unobserved down-dip widths, respectively. By working from the model of Chinnery (1964), our constant stress-drop model has the advantage of starting with realistic physics including the stress effects of surface rupture. Work remains to be done in comparing displacements predicted from our model with observations, but the fact that it fits the current magnitude-length-slip-rate data

as well or a bit better than the linear and bilinear models suggests that the constant stress-drop model is preferable to models that do not have this feature.

Data and Resources

The article "Total least squares" is available at https://en.wikipedia.org/wiki/Total_least_squares (last accessed February 2015).

Acknowledgments

The views and conclusions contained in this document are those of the authors and should not be interpreted as necessarily representing the official policies, either expressed or implied, of the U.S. Government.

References

Abercrombie, R. (1995). Earthquake source scaling relationships from -1 to 5 M_L using seismograms recorded at 2.5-km depth, *J. Geophys. Res.* **100,** 24,015–24,036.

Allen, C. R. (1975). Geological criteria for evaluating seismicity, *Bull. Geol. Soc. Am.* **86,** 1041–1057.

Allmann, B. P., and P. M. Shearer (2009). Global variations of stress drop for moderate to large earthquakes, *J. Geophys. Res.* **114,** no. B01310, doi: 10.1029/2008JB005821.

Anderson, J. G. (1986). Implication of attenuation for studies of the earthquake source, *Earthquake Source Mechanics, Maurice Ewing Series 6*, Geophysical Monograph 37, American Geophysical Union, Washington, D.C., 311–318.

Anderson, J. G., S. G. Wesnousky, and M. Stirling (1996). Earthquake size as a function of fault slip rate, *Bull. Seismol. Soc. Am.* **86,** 683–690.

Baltay, A., S. Ide, G. Prieto, and G. Beroza (2011). Variability in earthquake stress drop and apparent stress, *Geophys. Res. Lett.* **38,** L06303, doi: 10.1029/2011GL046698.

Baltay, A., G. Prieto, and G. C. Beroza (2010). Radiated seismic energy from coda measurements and no scaling in apparent stress with seismic moment, *J. Geophys. Res.* **115,** no. B08314, doi: 10.1029/2009JB006736.

Biasi, G. P., and S. G. Wesnousky (2016). Steps and gaps in ground ruptures: Empirical bounds on rupture propagation, *Bull. Seismol. Soc. Am.* **106,** 1110–1124, doi: 10.1785/0120150175.

Blaser, L., F. Krueger, M. Ohrnberger, and F. Scherbaum (2010). Scaling relations of earthquake source parameter estimates with special focus on subduction environment, *Bull. Seismol. Soc. Am.* **100,** 2914–2926.

Bormann, P., and D. Di Giacomo (2011). The moment magnitude M_w and the energy magnitude M_e: Common roots and differences, *J. Seismol.* **15,** 411–427.

Bormann, P., M. Baumbach, G. Bock, H. Grosser, G. L. Choy, and J. Boatwright (2005). Seismic sources and source parameters, in *New Manual of Seismological Observatory Practice (NMSOP)*, P. Bormann (Editor), Deutsches GeoForschungsZentrum GFZ, Potsdam, Germany, 1–94.

Bormann, P., S. Wendt, and D. Di Giacomo (2013). Seismic sources and source parameters, in *New Manual of Seismological Observatory Practice 2 (NMSOP2)*, P. Bormann (Editor), Chapter 3, Deutsches GeoForschungsZentrum GFZ, Potsdam, Germany, 1–259.

Byerlee, J. D. (1978). Friction of rocks, *Pure Appl. Geophys.* **116,** 615–626.

Castellaro, S., and P. Bormann (2007). Performance of different regression procedures on the magnitude conversion problem, *Bull. Seismol. Soc. Am.* **97,** 1167–1175, doi: 10.1785/0120060102.

Castellaro, S., F. Mulargia, and Y. Y. Kagan (2006). Regression problems for magnitudes, *Geophys. J. Int.* **165,** 913–930, doi: 10.1111/j.1365-246X.2006.02955.x.

Chinnery, M. A. (1963). The stress changes that accompany strike-slip faulting, *Bull. Seismol. Soc. Am.* **53,** 921–932.

Chinnery, M. A. (1964). The strength of the Earth's crust under horizontal shear stress, *J. Geophys. Res.* **59,** 2085–2089.

Dieterich, J. H. (1972). Time dependent friction in rocks, *J. Geophys. Res.* **20,** 3690–3704.

Goulet, C. A., N. A. Abrahamson, P. G. Somerville, and K. E. Wooddell (2015). The SCEC broadband platform validation exercise: Methodology for code validation in the context of seismic-hazard analyses, *Seismol. Res. Lett.* **86,** 17–26, doi: 10.1785/0220140104.

Graves, R., and A. Pitarka (2015). Refinements to the Graves and Pitarka (2010) broadband ground-motion simulation method, *Seismol. Res. Lett.* **86,** 75–80, doi: 10.1785/0220140101.

Hanks, T. C., and W. H. Bakun (2002). A bilinear source-scaling model for M-logA observations of continental earthquakes, *Bull. Seismol. Soc. Am.* **92,** 1841–1846.

Hanks, T. C., and W. H. Bakun (2008). M-logA observations for recent large earthquakes, *Bull. Seismol. Soc. Am.* **98,** 490–494.

Hanks, T. C., and W. H. Bakun (2014). M-logA models and other curiosities, *Bull. Seismol. Soc. Am.* **104,** 2604–2610, doi: 10.1785/0120130163.

Hanks, T. C., and H. Kanamori (1979). A moment magnitude scale, *J. Geophys. Res.* **84,** 2348–2350.

Hillers, G., and S. G. Wesnousky (2008). Scaling relations of strike-slip earthquakes with different slip-rate-dependent properties at depth, *Bull. Seismol. Soc. Am.* **98,** 1085–1101, doi: 10.1785/0120070200.

Ide, S., G. C. Beroza, S. G. Prejean, and W. L. Ellsworth (2003). Apparent break in earthquake scaling due to path and site effects on deep borehole recordings, *J. Geophys. Res.* **108,** 2271, doi: 10.1029/2001JB001617.

Iida, K. (1959). Earthquake energy and earthquake fault, Nagoya University, *J. Earth Sci.* **7,** 98–107.

Jiang, J., and N. Lapusta (2016). Deeper penetration of large earthquakes on seismically quiescent faults, *Science* **352,** 1293–1297.

Kanamori, H. (1977). The energy release in great earthquakes, *J. Geophys. Res.* **82,** 2981–2987.

Kanamori, H., and C. R. Allen (1986). Earthquake repeat time and average stress drop, in *Earthquake Source Mechanics*, S. Das, J. Boatwright, and C. H. Scholz (Editors), Geophysical Monograph 37, 227–235.

Kanamori, H., and D. L. Anderson (1975). Theoretical basis of some empirical relations in seismology, *Bull. Seismol. Soc. Am* **65,** 1073–1095.

King, G. C. P., and S. G. Wesnousky (2007). Scaling of fault parameters for continental strike-slip earthquakes, *Bull. Seismol. Soc. Am.* **97,** 1833–1840.

Leonard, M. (2010). Earthquake fault scaling: Self-consistent relating of rupture length, width, average displacement, and moment release, *Bull. Seismol. Soc. Am.* **100,** 1971–1988, doi: 10.1785/0120090189.

Leonard, M. (2012). Erratum to "Earthquake fault scaling: Self-consistent relating of rupture length, width, average displacement, and moment release," *Bull. Seismol. Soc. Am.* **102,** 2797.

Leonard, M. (2014). Self-consistent earthquake fault-scaling relations: Update and extension to stable continental strike-slip faults, *Bull. Seismol. Soc. Am.* **104,** 2953–2965, doi: 10.1785/0120140087.

Perrin, C., I. Manighetti, J.-P. Ampuero, F. Cappa, and Y. Gaudemer (2016). Location of largest earthquake slip and fast rupture controlled by along-strike change in fault structural maturity due to fault growth, *J. Geophys. Res.* **121,** 3666–3685, doi: 10.1002/2015JB012671.

Richins, W. D., J. C. Pechmann, R. B. Smith, C. J. Langer, S. K. Goter, J. E. Zollweg, and J. J. King (1987). The 1983 Borah Peak, Idaho, earthquake and its aftershocks, *Bull. Seismol. Soc. Am.* **77,** 694–723.

Rolandone, F., R. Burgmann, and R. M. Nadeau (2004). The evolution of the seismic-aseismic transition during the earthquake cycle: Constraints

from the time-dependent depth distribution of aftershocks, *Geophys. Res. Lett.* **31**, L23610, doi: 10.1029/2004GL021379.

Sato, R. (1972). Stress drop for a finite fault, *J. Phys. Earth* **20**, 397–407.

Scholz, C. H. (1982). Scaling laws for large earthquakes: Consequences for physical models, *Bull. Seismol. Soc. Am.* **72**, 1–14.

Scholz, C. H. (2002). *The Mechanics of Earthquakes and Faulting*, Second Ed., Cambridge University Press, Cambridge, United Kingdom, 471 pp.

Scholz, C. H., C. A. Aviles, and S. G. Wesnousky (1986). Scaling differences between large intraplate and interplate earthquakes, *Bull. Seismol. Soc. Am.* **76**, 65–70.

Shaw, B. E. (2009). Constant stress drop from small to great earthquakes in magnitude-area scaling, *Bull. Seismol. Soc. Am.* **99**, 871–875.

Shaw, B. E., and C. H. Scholz (2001). Slip-length scaling in large earthquakes: Observations and theory and implications for earthquake physics, *Geophys. Res. Lett.* **28**, 2995–2998.

Shaw, B. E., and S. G. Wesnousky (2008). Slip-length scaling in large earthquakes: The role of deep-penetrating slip below the seismogenic layer, *Bull. Seismol. Soc. Am.* **98**, 1633–1641.

Strasser, F. O., M. C. Arango, and J. J. Bommer (2010). Scaling of the source dimensions of interface and intraslab subduction-zone earthquakes with moment magnitude, *Seismol. Res. Lett.* **81**, no. 6, 941–950.

Tocher, D. (1958). Earthquake energy and ground breakage, *Bull. Seismol. Soc. Am.* **48**, 147–153.

Wells, D. L., and K. J. Coppersmith (1994). New empirical relationships among magnitude, rupture length, rupture width, rupture area, and surface displacement, *Bull. Seismol. Soc. Am.* **84**, 974–1002.

Wesnousky, S. G. (1988). Seismological and structural evolution of strike-slip faults, *Nature* **335**, 340–343.

Wesnousky, S. G. (1999). Crustal deformation processes and the stability of the Gutenberg-Richter relationship, *Bull. Seismol. Soc. Am.* **89**, 1131–1137.

Wesnousky, S. G. (2008). Displacement and geometrical characteristics of earthquake surface ruptures: Issues and implications for seismic-hazard analysis and the process of earthquake rupture, *Bull. Seismol. Soc. Am.* **98**, 1609–1632.

Wesnousky, S. G., C. H. Scholz, and K. Shimazaki (1983). Earthquake frequency distribution and the mechanics of faulting, *J. Geophys. Res.* **88**, 9331–9340.

Appendix

Fault-Scaling Relations

Basics

This article proposes models to estimate the moment magnitude of earthquakes based on observed surface rupture lengths and slip rates. The moment magnitude definition that we use is implicit in Kanamori (1977):

$$M_\mathrm{w} = \frac{2}{3}\left(\log M_0 - 16.1\right). \tag{A1}$$

The units of seismic moment M_0 are dyn·cm in equation (A1). This definition differs slightly from the equation used by Hanks and Kanamori (1979) but is the equation recommended for seismic network operations by the International Association of Seismology and Physics of the Earth's Interior since 2005 (see Bormann *et al.*, 2005, 2013; Bormann and Di Giacomo, 2011; and references therein), and thus is the relationship used by most seismic networks throughout the world. The seismic moment is defined as

$$M_0 = \mu A_E \bar{D}_E = \mu L_E W_E \bar{D}_E, \tag{A2}$$

in which μ is the shear modulus, A_E is the fault area ruptured in the earthquake, and $\bar{D}_E$ is the average slip over that area. For a fault that is approximately rectangular $A_E = L_E W_E$, in which L_E is the rupture length measured along strike and W_E is the down-dip rupture width.

Substituting equation (A2) into (A1), one obtains (for cgs units)

$$M_\mathrm{w} = \frac{2}{3}\log L_E + \frac{2}{3}\log W_E + \frac{2}{3}\log \bar{D}_E + \frac{2}{3}(\log \mu - 16.1). \tag{A3}$$

This justifies the models that relate magnitude to the log of fault length, width, and mean slip. Slopes different from 2/3 result from correlations among the fault parameters L_E, W_E, and $\bar{D}_E$. Wells and Coppersmith (1994) found that the model

$$M_\mathrm{w} = c_1 \log L_E + c_0 \tag{A4}$$

predicts magnitude from rupture length with a standard deviation of the misfit $\sigma_1 = 0.28$.

The possible dependence of stress drop or magnitude on slip rate was recognized by Kanamori and Allen (1986) and Scholz *et al.* (1986). With the addition of the slip-rate term, equation (A4) becomes, used by Anderson *et al.* (1996; hereafter, AWS96):

$$M_\mathrm{w} = c_0 + c_1 \log L_E + c_2 \log S_F. \tag{A5}$$

Testing for a logarithmic dependence on the geological fault-slip rate S_F can be motivated by findings in Dieterich (1972). In this article, equation (A5) is equivalent to model M1.

Constant Stress-Drop Scaling

The static stress drop $\Delta\tau_S$ is the average decrease in the shear stress acting on the fault as a result of the earthquake and is proportional to the ratio of average slip to a fault dimension. Seismic observations have found that the average value of $\Delta\tau_S$ is approximately constant ($\sim$4 MPa, $\sim$40 bars) over a broad range of earthquake magnitudes (e.g., Kanamori and Anderson, 1975; Allmann and Shearer, 2009), although there is considerable scatter in these data. Seismic moment, and thus M_w through equation (A1), can be expressed as a function of fault dimension and stress drop, as recognized by Kanamori and Anderson (1975). Selected models are summarized in Table A1.

The equations in Table A1 indicate that constant stress drop implies the slope $c_1 = 2.0$ for small faults (first case 1) when L_E is equated to the diameter of the circular fault and $c_1 = 2/3$ for long faults (second and third cases). These observations motivate a bilinear approach to fit the data, which is model M2 in this article. The bilinear approach is formulated as follows:

Table A1
Models from Kanamori and Anderson (1975) for the Relationship of Fault Size, Stress Drop, and M_{w}

Case	M_0	Implied Magnitude Relations*
Buried, circular	$\frac{16}{7}\Delta\tau_S R_E^3$	$M_{\mathrm{w}} = \log A_E + \frac{2}{3}\log\Delta\tau_S + 3.0089$
		If $L_E = 2R_E$: $M_{\mathrm{w}} = 2\log L_E + \frac{2}{3}\log\Delta\tau_S + 2.904$
Strike slip, long	$\frac{\pi}{2}\Delta\tau_S W_E^2 L_E$	$M_{\mathrm{w}} = \frac{2}{3}\log L_E + \frac{4}{3}\log W_E + \frac{2}{3}\log\Delta\tau_S + 3.1359$
Dip slip, long	$\frac{\pi(\lambda+2\mu)}{4(\lambda+\mu)}\Delta\tau_S W_E^2 L_E$	$M_{\mathrm{w}} = \frac{2}{3}\log L_E + \frac{4}{3}\log W_E + \frac{2}{3}\log\Delta\tau_S + 3.3141$

*$A_E = \pi R_E^2$, fault area in km^2; R_E, fault radius; W_E, fault width; and L_E, fault length in km, and $\Delta\tau_S$, stress drop in bars.

$$M_{\mathrm{w}} = M_{\mathrm{bp}} + c_{1C}\log\left(\frac{L_E}{L_{\mathrm{bp}}}\right) + c_2\log\left(\frac{S_F}{S_0}\right) \quad L_E < L_{\mathrm{bp}}$$

$$M_{\mathrm{w}} = M_{\mathrm{bp}} + c_{1L}\log\left(\frac{L_E}{L_{\mathrm{bp}}}\right) + c_2\log\left(\frac{S_F}{S_0}\right) \quad L_E \geq L_{\mathrm{bp}}, \quad \text{(A6)}$$

in which the length L_{bp} is the length at which the length dependence of the scaling relationship changes from the small fault model with slope $c_{1C} = 2$ to the long fault model with slope $c_{1L} = 2/3$. The slip rate S_0 is a reference slip rate which can be chosen arbitrarily, but is conveniently chosen to be the log average slip rate in the data, so that setting $S_F = S_0$ gives the best fit when slip rate is unknown. The constant M_{bp} is the magnitude corresponding to a fault with length $L_E = L_{\mathrm{bp}}$ and slip rate $S_F = S_0$. Equation (A6) has three unknown coefficients (M_{bp}, L_{bp}, and c_2), which is the same number as in equation (A5).

However, there are issues with the applicability of the equations in Table A1. The foremost, for the long faults, is the width of the seismogenic zone. Table A1 shows that W_E is twice as influential as the fault length, so it needs to be considered carefully. One approach to estimate this width is to use the maximum depth of microearthquakes. By this approach, for strike-slip earthquakes the maximum depth of microearthquakes equates directly to an estimate of the fault width, whereas for a reverse or normal fault the dip is incorporated. The problem is that the maximum depth of seismogenic rupture in large earthquakes is difficult to observe. King and Wesnousky (2007) discuss this difficulty and present arguments for why the down-dip width might be larger in large earthquakes, at least up to some limit greater than that inferred from the depth range of small earthquakes, because rocks below the depths of mircoearthquakes might experience brittle failure under high strain rates. If the width increases in general for long ruptures, stress drop is no longer as high for these events because stress drop is inversely proportional to W_E, and furthermore the slope c_1 can no longer be reliably constrained by the models in Table A1. King and Wesnousky (2007) propose that this explains the proposal by Scholz (1982) that slip in large earthquakes is more nearly proportional to rupture length than to rupture width.

Another issue is that the first equation in Table A1 assumes that the circular fault is confined within the Earth and thus neglects free surface effects, while by definition all of the events considered in this study rupture the surface. This motivates the development of the model that is described in the next section.

Relations Based on Chinnery (1964)

Chinnery (1963, 1964) calculated a stress drop for a rectangular strike-slip fault that ruptures the surface. Unlike the circular slip model, the free surface in the Chinnery model is present for small earthquakes. His equations assume a uniform slip on the fault. Thus, the stress drop is variable over the fault and becomes singular at the edge of the fault. His equations give the stress drop on the surface at the midpoint of the rupture. Numerical solutions in Chinnery (1963) show relatively uniform stress drop over large portions of the fault. Chinnery (1963) thus suggests that the results are valid to represent the fault stress drop so long because the zone of slip fall-off is much smaller than the area of the fault. The key advantage provided by this approach is to provide a useful analytical solution.

For the rectangular fault with length L_E, width W_E, and aspect ratio $C_{LW} = L_E/W_E$, the stress drop in the Chinnery model $\Delta\tau_C$ at the midpoint at the surface is

$$\Delta\tau_C = \frac{\mu\bar{D}_E}{2\pi}C_1(L_h, W_E), \quad \text{(A7)}$$

in which

$$C_1(L_h, W_E) = \left\{\frac{2L_h}{aW_E} + \frac{3}{L_h} - \frac{L_h(3a + 4W_E)}{a(a + W_E)^2}\right\}. \quad \text{(A8)}$$

Note that $L_h = L_E/2$ and $a = (L_h^2 + W_E^2)^{1/2}$. Observe that C_1 has dimensions of $1/\text{length}$, and thus C_1^{-1} is effectively the fault dimension that is used for calculating the strain. In other words, the strain change in the earthquake is $\sim\bar{D}_E C_1$. An equation for the seismic moment can be obtained by solving equation (A7) for $\bar{D}_E$ and substituting in equation (A2). The result is

$$M_0 = 2\pi\Delta\tau_C\frac{L_E W_E}{C_1(L_h, W_E)} \quad \text{(A9)}$$

and thus

$$M_{\mathrm{w}} = \frac{2}{3}\log L_E + \frac{2}{3}\log\Delta\tau_C + \frac{2}{3}\log\frac{2\pi W_E}{C_1(L_h, W_E)} - \left(\frac{2}{3}\right)16.1. \quad \text{(A10)}$$

Additional insight into the geometrical term can be obtained by observing that a is the length of the diagonal from the midpoint of the fault at the surface to either of the bottom corners. If the dip of this line is γ, then $\tan\gamma = W_E/L_h = 2/C_{LW}$, $L_h = a\cos\gamma$, $W_E = a\sin\gamma$, and one can rewrite

$$C_1(L_h, W_E) = \frac{1}{W_E}C(\gamma), \quad \text{(A11)}$$

in which

$$C(\gamma) = 2\cos\gamma + 3\tan\gamma - \frac{\cos\gamma\sin\gamma(3 + 4\sin\gamma)}{(1 + \sin\gamma)^2}. \quad (A12)$$

Thus, one can rewrite equation (A7) as

$$\Delta\tau_C = \frac{C(\gamma)}{2\pi}\mu\frac{\bar{D}_E}{W_E}. \quad (A13)$$

Solving equation (A13) for $\bar{D}_E$ and substituting into equation (A2) gives the moment of a vertical strike-slip fault that ruptures the surface as

$$M_0 = \frac{2\pi}{C(\gamma)}\Delta\tau_C L_E W_E^2. \quad (A14)$$

Because γ, and thus $C(\gamma)$, depends on the fault aspect ratio, equations (A9) or (A14), can be used to model a transition from small-earthquake behavior (e.g., the circular fault in Table A1) to a long-fault behavior. This article, similar to Hanks and Bakun (2002), maintains a constant aspect ratio as the fault length increases, until that aspect ratio implies that the fault width would exceed some maximum. For longer faults, the width is set to that maximum. Before reaching that maximum, γ and $C(\gamma)$ are constant, and

$$M_0 = \frac{2\pi}{C(\gamma)}\Delta\tau_C\frac{L_E^3}{C_{LW}^2} \quad \frac{L_E}{C_{LW}} < W_{\max}. \quad (A15)$$

For longer faults, for which the width is limited, equation (A14) becomes

$$M_0 = \frac{2\pi}{C(\gamma)}\Delta\tau_C L_E W_{\max}^2 \quad \frac{L_E}{C_{LW}} \geq W_{\max}. \quad (A16)$$

In this case, as the fault length increases while width is held constant, γ will be decreasing. For the limit of small γ (roughly $\gamma \lesssim 25°$), equation (A12) shows that $C(\gamma) \to 2$, so equation (A9) approaches

$$M_0 = \pi\Delta\tau_C L_E W_{\max}^2. \quad (A17)$$

Equation (A17) differs from the second case in Table A1 for the long strike-slip fault by a factor of 2 ($\Delta\tau_S = 2\Delta\tau_C$), in which the difference is due to the different boundary conditions used for the two solutions at depth.

From equations (A15) and (A16), converting to magnitude, the implied scaling relationship based on the Chinnery model is

$$M_w = \begin{cases} 2\log L_E + \frac{2}{3}\log\Delta\tau_C + \frac{2}{3}\left(\log\frac{2\pi}{C_{LW}^2 C(\gamma)} - 16.1\right) & \frac{L_E}{C_{LW}} < W_{\max} \\ \frac{2}{3}\log L_E + \frac{2}{3}\log\Delta\tau_C + \frac{2}{3}\left(\log\frac{2\pi W_{\max}^2}{C(\gamma)} - 16.1\right) & \frac{L_E}{C_{LW}} \geq W_{\max}. \end{cases}$$
$$(A18)$$

Equation (A18) will be the third model M3 considered in this study, with the addition of a slip-rate contribution $+c_2\log(S_F/S_0)$, to the two branches of the equation. The
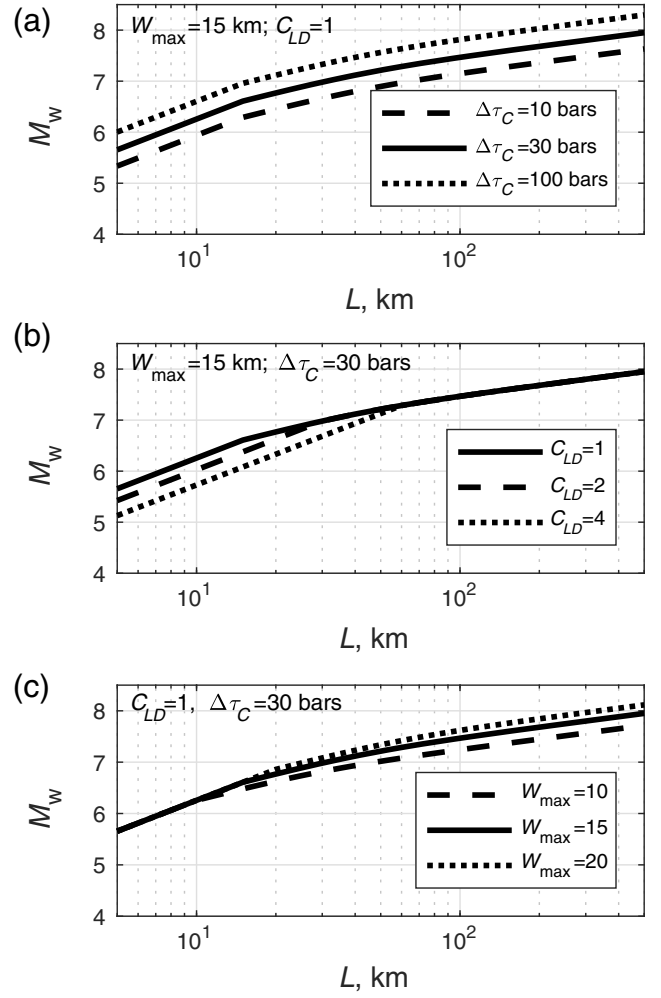
Figure A1. Model for M_w based on the Chinnery (1964) scaling as given in equation (A18). (a) Effect of changing the stress drop $\Delta\tau_C$. (b) Effect of changing the aspect ratio of the fault. (c) Effect of changing the limiting rupture width $W_{\max}$.

unknown parameters in model M3 are $\Delta\tau_C$, C_{LW}, $W_{\max}$, and c_2. Thus, this model has four parameters to be determined, compared with three parameters in models M1 and M2. Figure A1 shows the effect of the three parameters $\Delta\tau_C$, C_{LW}, and $W_{\max}$ on magnitude predictions. The stress drop scales the entire curve upward. The aspect ratio C_{LD} adjusts the level of the magnitude for short rupture lengths. The maximum width affects the curvature and how rapidly the curve approaches the asymptotic slope of $(2/3)\log L_E$ for long rupture lengths.

Other Models and Considerations

Sato (1972) overcomes the singularity introduced by Chinnery (1963, 1964) by assuming a smooth *ad hoc* slip function on a finite rectangular/elliptical-shaped fault, and for that function, calculating the average stress drop resulting from that slip function. Although the results are informative for source physics studies, the major disadvantages of this

approach for our application are that the fault is embedded in a whole space, and there is no analytical solution comparable to equation (A7). Rather, the geometrical factor equivalent to $C(\gamma)$ can be computed numerically using equations in Sato (1972) or read from a figure in the paper. Considering these limitations, this model was not considered further.

Shaw and Scholz (2001) and Shaw and Wesnousky (2008) implement a numerical model for fault slip in a half-space with depth-dependent friction. They examine the statistics of events that rupture the surface. These papers are interesting for the finding that large surface-rupturing events also slip below the brittle crustal depths. The scaling found in the model has properties similar to the scaling in the Chinnery model. However, the scaling relationship that they determine has an *ad hoc* shape, and thus we preferred the analytical functional form of equation (A18). The physics-based solution of Chinnery was also preferred to a related constant stress-drop model by Shaw (2009). This model proposes three regimes of magnitude scaling from length based on intermediate length–width–displacement–scaling relations and heuristic arguments for transitions between them.

Rolandone *et al.* (2004) found some empirical evidence that might be interpreted to support the penetration of rupture below the brittle seismogenic layer in large earthquakes. They found that the maximum depth of aftershocks of the Landers earthquake were deeper immediately after the mainshock, and then the maximum depth returned to pre-earthquake levels over the next few years. This might be explained by high strain rates in the uppermost part of the ductile crust, as high strain rates favor brittle failure. However, postseismic strain rates in that depth range would be high even if seismic rupture of the mainshock did not extend that deep, so these observations allow, but do not require, dynamic rupture below the long-term average depth of microearthquakes.

Nevada Seismological Laboratory
University of Nevada
Reno, Nevada 89557
jga@unr.edu
stevew@seismo.unr.edu